From Electric Doping Control to Thermal Defect Nucleation in Perovskites

Stefan Marinković* Alejandro Fernández-Rodríguez Emile Fourneau Mariona Cabero Hailin Wang Ngoc Duy Nguyen Jaume Gazquez Narcís Mestres Anna Palau Alejandro V. Silhanek*

S. Marinković[1], E. Fourneau, Prof. A. V. Silhanek[2]
Experimental Physics of Nanostructured Materials, Q-MAT, CESAM, Université de Liège, B-4000 Sart Tilman, Belgium
[1]smarinkovic@uliege.be [2]asilhanek@uliege.be
A. Fernández-Rodríguez, H. Wang, J. Gazquez, N. Mestres, A. Palau
Institut de Ciència de Materials de Barcelona, ICMAB-CSIC, Campus UAB, 08193 Bellaterra, Spain
E. Fourneau, Prof. N. D. Nguyen
Solid-State Physics - Interfaces and Nanostructures, Q-MAT, CESAM, Université de Liège, B-4000 Sart Tilman, Belgium
M. Cabero
Centro Nacional de Miscroscopía Electrónica de la Universidad Complutense de Madrid, 28040 Madrid, Spain

Simultaneous optical microscopy and electric transport measurements on $La_{0.7}Sr_{0.3}MnO_3$ (LSMO) nanobridges, grown on $SrTiO_3$ (STO), show direct evidence of directional oxygen vacancy migration under large voltage bias. Comparative study on discontinuous structures, with voltages applied across a micron-scale gap, demonstrates that high electric fields induce electrolytic modifications confined to the anode. Extensive electromigration is shown to induce the formation of linear surface scars on the STO substrate, following well defined crystallographic directions. We demonstrate the reproducible triggering of these surface dislocations, unveil their thermal rather than electrical origin and show that they do not represent electroformed conduction channels. High-resolution Scanning Transmission Electron Microscopy (STEM) imaging reveals that the scars correspond to nanometer scale steps caused by (101) gliding planes in the STO caused by the proliferation of edge dislocations and local lattice expansion. These findings shed light on selective electrically-controlled atom migration and its role in structural modification of functional oxides, opening a unique avenue for ionotronic device design.

1 Introduction

Transition metal oxides are well studied for their functionalities as memristive devices,[1,2] heterogeneous catalysts,[3] and electrode materials for solid oxide fuel cells.[4] Among all available materials, manganites display some of the most interesting physical effects,[5] being model systems for the study of magnetoresistance[6] and holding large potential in ionotronic and spintronic applications.[7]

Particular interest has been devoted to non-stoichiometric oxygen-deficient perovskite oxides, in part due to the modification of their cationic valence states following changes in oxygen vacancy concentration.[8,9] This adaptation of the metal charge state has a profound effect on the magnetic, electric and structural response of the system. Since oxygen ions and vacancies can be displaced over distances of several μm by sufficiently strong electric fields, an all-electrical control of the above-listed properties can be envisaged.[10]

Amidst these perovskite-type oxides, $La_{1-x}Sr_xMnO_{3-\delta}$ (LSMO) occupies a privileged place as the most studied manganite, greatly due to its magnetoresistive and resistance-switching behavior, as well as the close relationship of its conductive and magnetic response to crystal structure. Substituting La^{3+} by Sr^{2+} oxidizes Mn^{3+} into Mn^{4+}, resulting in a mixed valence of Mn ions in the unit cell[9] and the material's non-stoichiometry. As x increases, a double exchange interaction between Mn ions bridged by oxygen[11] dictates the electronic distribution leading to the development of a ferromagnetic phase at low temperatures. This phase has a Curie temperature reaching a maximum of $T_C \approx 370$ K for $x \approx 0.33$. In this system, magnetism and conduction are intimately coupled: when the magnetic moments are misaligned (i.e. the material is in the paramagnetic state), electrons cannot be transferred by means of a double exchange mechanism, and hence a decrease of resistivity is associated with spin-alignment. With increasing oxygen deficiency δ, the average Mn oxidation state decreases and thus the average Mn ionic size increases. As a result, the lattice

parameter of manganese oxide increases and both the Curie temperature and the magnetization decrease whereas the resistivity increases.[12]

After recognizing the importance of the oxygen distribution in the material and its anisotropic atomic mobility characteristic of perovskites, there were several attempts at demonstrating the thermoelectrically induced migration of vacancies in LSMO on STO. Balcells et al.[13] showed that at high current densities ($> 10^5$ Acm^{-2}), the depletion of oxygen content promotes irreversible changes in the samples with a remarkable increase of resistance and a reduction of the ferromagnetic transition temperature. Recently, further evidence suggesting the displacement of oxygen vacancies under the combined effect of electric field and Joule heating has been reported.[14–17] Even though voltage induced phase changes were observed at the microscopic level by means of Scanning Transmission Electron Microscopy (STEM) by Yao et al.,[18] unambiguous macroscopic evidence of electrically stimulated oxygen vacancy migration has not been provided as of yet.

In this work, we use concurrent optical microscopy and electrical transport measurements to asses the oxygen vacancy distribution in LSMO nanobridges, epitaxially grown on STO substrates, under controlled electrical stress in ambient and cryogenic conditions. Evidence is provided of directional oxygen flow under large voltage bias, which is then compared to the behaviors of discontinuous (gapped) structures. For the latter, a distinctly electrolytic behavior is observed. Strikingly, a peculiar structural feature suddenly emerges upon extended electromigration: superficial scars as linear defects spreading from the LSMO nanobridge outwards along the crystallographic directions of the substrate. Electrical characterization, scanning electron microscopy (SEM), atomic force microscopy (AFM), conductive AFM (c-AFM), as well as STEM are used to assess the effects of electro-thermally driven oxygen migration on the structural stability of the system. Our findings demonstrate the possibility to achieve all-electrical and targeted generation of dislocations in post-synthesized on-chip structures in the path towards new ionic functional devices.

2 Results and discussion

2.1 Directional migration of oxygen in LSMO

The 20 nm-thick LSMO films investigated in this work exhibit a metal-insulator transition and a Curie temperature above room temperature evidenced by the temperature dependent magnetization $M(T)$ and the resistance $R(T)$ shown in **Figure 1**(a,b). The presence of the low-temperature ferromagnetic phase is directly confirmed by the magneto-optical image shown in the inset of panel (a) obtained at 5 K with an in-plane field of 3 mT. Similar magnetic field landscape is obtained at room temperature. Two different geometrical sample designs have been measured: (i) a continuous, multiprobe structure consisting of a narrow central LSMO bridge symmetrically surrounded by wider bridges, each bridge individually addressable by corresponding voltage contacts as shown in Figure 1(c), and (ii) a discontinuous, mirror symmetric structure, as shown in Figure 1(d), separated by a gap of 3, 7, or 15 μm.

The multiterminal bridge shown in Figure 1(c) permits us to electrically unveil the directional displacement of oxygen. To that end, current pulses of 1 s duration at ambient conditions are applied across the entire device with the polarity as indicated by the sketch in **Figure 2**(b). Figure 2(a-c) show the relative resistance change ΔR at each junction with respect to the resistance of the pristine state, as a function of temperature. These panels are color-coded as indicated in the sketch in Figure 2(b). The first three pulses are of same amplitude, i.e. 0.5 mA, whereas the last one is doubled to 1 mA. The resistance as a function of temperature $R(T)$ is measured after every pulse for all junctions simultaneously with a current of 100 nA RMS, using a lock-in amplifier.

Although optical images taken before and after the pulses do not exhibit any hint of modification on the constrictions, the gathered electrical data shows evidence of directional mass transport. Electro-pulsing induces an increase of resistance on the left bridge and a corresponding decrease on the right one. This behavior is consistent with oxygen vacancies displacing from anode (+) to cathode (-) since increasing oxygen deficiency δ leads to an increase in resistivity.[12] Note that the central bridge remains mostly
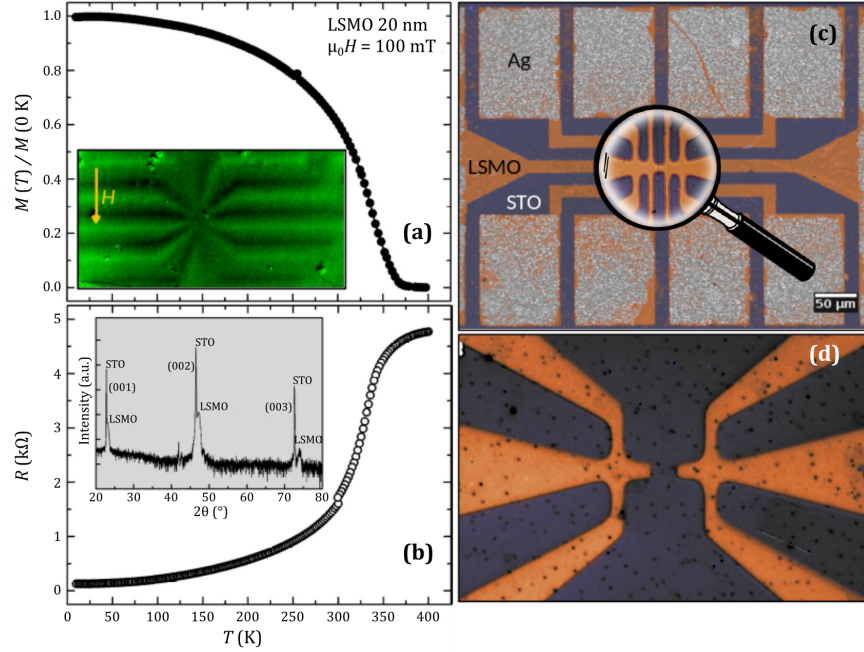
Figure 1: Normalized magnetization (a) and resistance (b) as a function of temperature for a 20 nm thick plain film of LSMO. The ferromagnetic-paramagnetic transition takes place at a Curie temperature $T_C \approx 370$ K and is accompanied by a metal-insulator transition. The inset in panel (a) shows a 5 K magneto-optical image of the stray field generated by the sample shown in panel (c) with an in-plane magnetic field $H = 3$ mT. The inset in panel (b) corresponds to the X-ray diffraction spectra of a plain LSMO film deposited on STO substrate. SEM images of the two investigated sample layouts (continuous and discontinuous) are shown in panels (c) and (d), respectively. The zoom-in in panel (c) with a magnifying glass shows an optical microscopy image of the three bridges, the central one being $1\times3\ \mu\text{m}^2$. In panel (d) the gap separating the two mirror symmetric structures is 3 μm.

invariant after the pulses and that for all three bridges the resistance changes are almost imperceptible below 50 K.

We have demonstrated recently that the increased reflectivity of oxygen deficient $\text{YBa}_2\text{Cu}_3\text{O}_{7-\delta}$ offers the possibility to visualize the vacancy distribution as they diffuse under electrical stress.[19] A similar phenomena could be expected in LSMO, considering the fact that both materials are perovskite-like structured ceramic oxides. In order to induce longer range oxygen vacancy displacements and image the diffusion process in situ at 110 K, we submitted the sample to a series of voltage pulses of linearly growing amplitude as schematically shown in **Figure 3**(a). Before and after each pulse, the resistance of the sample is monitored and optical images are acquired. The voltage amplitude and the current circulating through
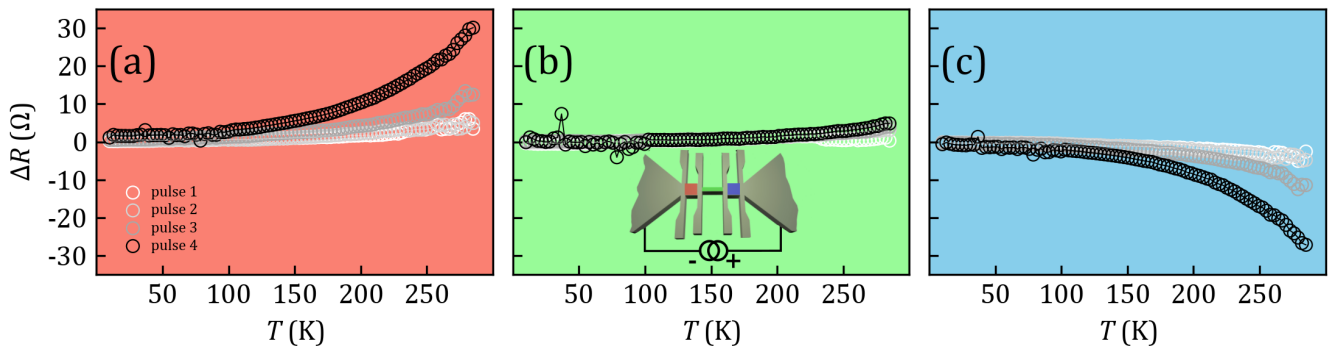

Figure 2: Relative change of resistance $\Delta R = R_i - R_0$, with R_i obtained after i-th current pulse and R_0 the resistance in the pristine state, as a function of temperature. The first three pulses are of same amplitude 0.5 mA whereas the fourth and last pulse increases to 1 mA. The background color of each panel indicates the corresponding transport bridge as illustrated in the sketch of panel (b).
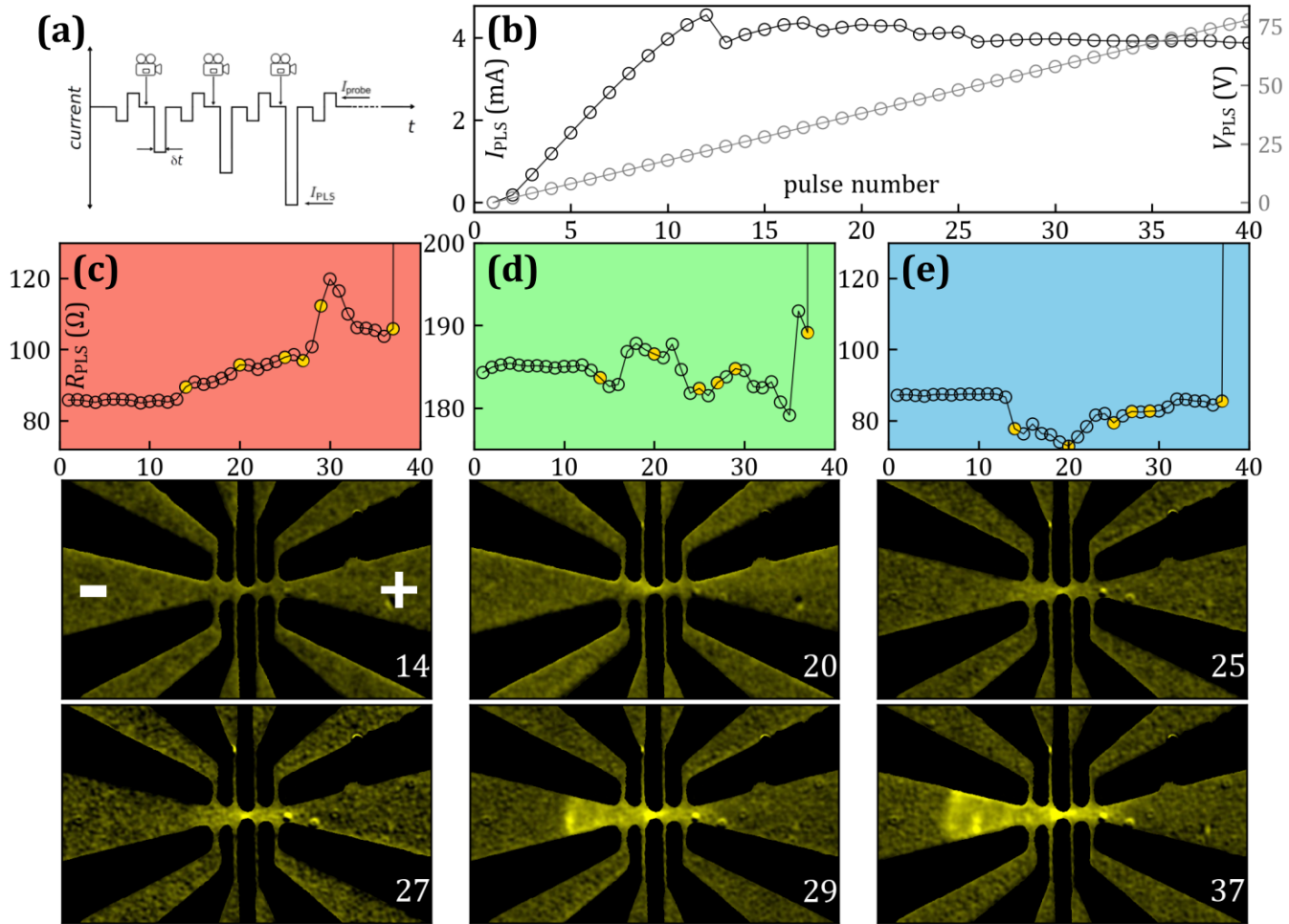
Figure 3: (a) A bipolar I_{probe} pulsed current is used to monitor the sample resistance whereas a $I_{PLS} \gg I_{probe}$ of variable amplitude resulting from linearly increasing voltage pulses (b) triggers the oxygen migration process. Resistance of the left (c), central (d), and right (e) bridges after the voltage pulse as a function of the pulse number. The lower two rows show optical microscopy images acquired after the pulse number indicated in the frame. Electric transport and microscopy imaging are acquired at a bath temperature of 110 K.

the device in response to the voltage pulses, as a function of pulse number (or time) are plotted in Figure 3(b).

The current I_{PLS} initially increases linearly as a consequence of a nearly invariant resistance. For higher amplitude of voltage pulses the current seems to saturate in a plateau value of ~ 4 mA indicating a resistance growing roughly linearly with the applied voltage. The resistance of each bridge as a function of pulse number is shown in panels (c-e) with an excitation respecting the same polarity as shown by the sketch in Figure 2(b). Consistent with the previous observation, the resistance of the individual bridges remains constant up to pulse number 12 and undergo modification for higher pulse numbers. A selected set of optical images is shown in the lower two rows of Figure 3 in which the corresponding pulse number is indicated. Up to pulse number 14 no apparent changes in reflectivity are discerned. However, starting from pulse number 20, a clear progressing front of increased reflectivity advances towards the cathode. To the best of our knowledge, this is the first direct visualization of electrically-driven macroscopic migration of oxygen vacancies in LSMO.

2.2   Generation of Crystallographic Defects in the LSMO/STO System

The resistance of the measured device increases abruptly around pulse number 37, as is shown in Figure 3(c-e). A close inspection of the optical images before (**Figure 4**(a)) and after (Figure 4(b)) this transition

reveals the formation of lines extending across both the substrate and the LSMO nanobridges, notably along well defined crystallographic directions [100] and [010] of the STO. This effect has been observed in all samples under significant electro-pulsing stress. The pristine sample shown in Figure 4(a) is absent of lines, whereas for the electrically stressed sample in panel (b), two vertical lines and an horizontal line are indicated with white arrows. Inspection of the sample by scanning electron microscopy shown in Figure 4(c) reveals further details. Indeed, this image has been acquired with a Everhart-Thornley secondary-electron detector, giving mostly topographic contrast. The fact that the vertical line at the left appears dark whereas the line at the right side appears bright, suggests that the left line is a step down and the right line is a step up. Step heights can be quantified with higher z-resolution by AFM, as shown in Figure 4(d-h). Panels (d) and (e) show two scan areas of $8 \times 8 \ \mu m^2$, and the line profiles **A-A'** and **B-B'** are shown in panels (f) and (g), respectively. The measurements indicate that the whole structure undergoes a decrease in height of about 15 nm in between the the vertical streaks shown in panel (b). The profile **B-B'** taken at the substrate shows that indeed this structural defect propagates and likely originates on the STO substrate. Panel (h) presents a tilted three-dimensional view of panel (e) for better visualization of the trench produced in the sample. The steps seemingly align well-defined crystallographic orientations of the STO substrate.

Electric-field triggered structural transformation in STO has been reported by Hanzig et al.,[20] who showed that the out-of-plane lattice parameter increases by increasing the electric field up to few MVm^{-1}. High electric field combined with high temperature induces migration of oxygen vacancies along the local
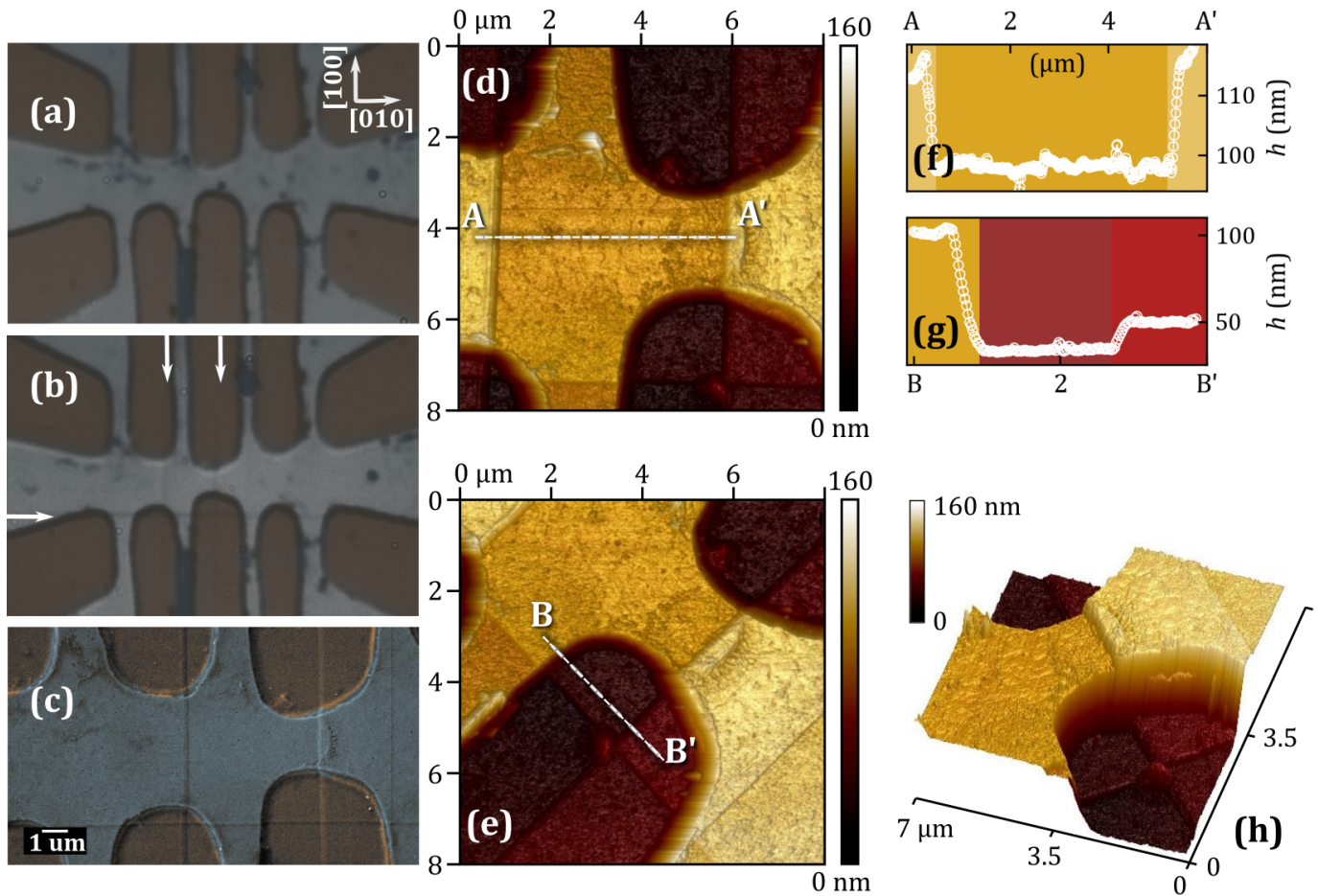

Figure 4: Bright-field optical microscopy images of the LSMO/STO sample in the pristine state (a) and after applying a high electro-thermic stress (b) at bath temperature of 110 K. In (b) the appearance of dark vertical and horizontal lines in the substrate are indicated with white and black arrows, respectively. In (c) a scanning electron microscopy image of the central and left bridges is shown. Atomic force microscopy images of the same sample are shown in panels (d), (e) and (h). The line profiles indicated by the segments **A-A'** and **B-B'** are shown in panel (f) and (g), respectively.
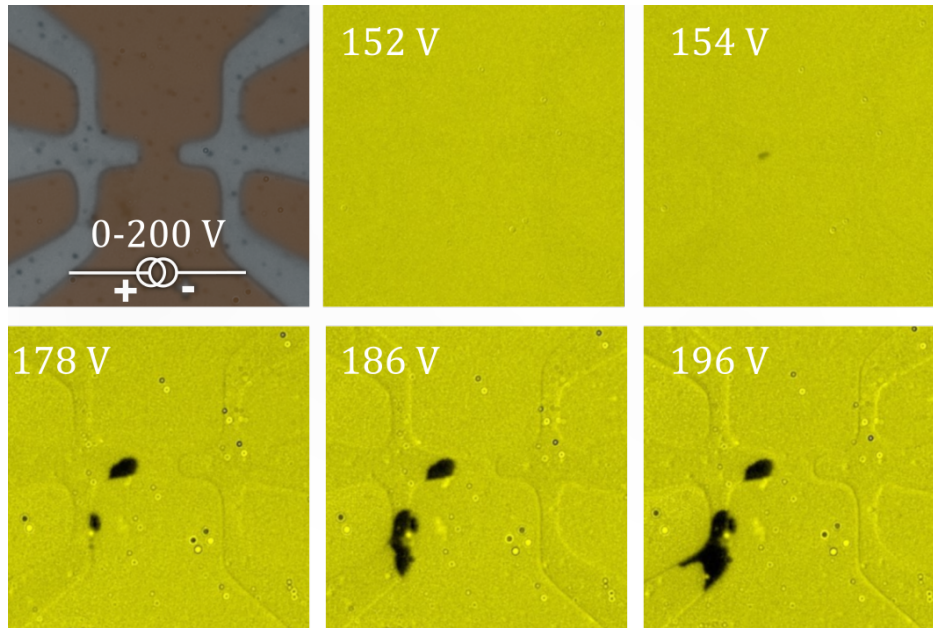
Figure 5: Upper left panel: Optical microscopy image of the measured device and the polarity of the sweeping voltage ranging from 0 to 200 V at ambient conditions. The narrowest gap between the two electrodes is 3 μm. Yellowish background panels show differential images for which the image of the pristine sample has been subtracted to that of the indicated voltage. An area of electrolyzed LSMO can be observed developing above 154 V.

chemical and electric potential,[21] which in turn causes a cation (Sr, Ti) counterflow maintaining charge neutrality. This redistribution of mobile species reduces the stability of the crystal structure. A reversible electric field-induced structural change in the near-surface region of STO has also been reported through X-ray absorption measurements by Leisegang et al.[22] using calculated Ti valence as a proxy for the oxygen vacancy distribution. More recently, Bobeth et al.,[23] Szot et al.,[24] Waser et al.,[25] and Rodenbucher et al.[26] have shown via X-ray scattering measurements that well-oriented streaks along the [100] axis of the STO crystal, 1 to 10 μm in diameter, emerge from the cathode and propagate towards the anode during what is known as the electroformation process. These authors demonstrate that these streaks do not propagate on the surface, but are situated within a skin region 100 μm below the surface. Upon connecting the electrodes by these streaks, the resistance suddenly drops suggesting the development of a pipe diffusion conduction mechanism. In contrast to this, crystallographic edge dislocations in STO have shown no evidence of pipe diffusion and the consequent improvement of ionic transport.[27,28]

The fact that the observed lines are crystallographically oriented superficial scars on the STO, rapidly developing irrespective of the voltage polarity, points to a different phenomena than the streaks reported in Ref.[24] Further evidence can be obtained by using two separate electrodes (i.e. a well-defined anode-cathode system) and attempting to trigger streaks by increasing the electric potential difference between them. The sample layout shown in Figure 1(d) was used and exposed to a linearly increasing voltage bias regime as schematically shown in the top left panel of **Figure 5**, while optical images were taken at each voltage step. A selected set of images for which the pristine state has been subtracted to improve the contrast, is shown in Figure 5. From zero up to a potential difference of 152 V no effect is observed in the structure. At 154 V, the sample changes its reflectivity (darkens) on the anode side (+) and remains unchanged on the cathode side (-). The affected area keeps growing as voltage increases until 172 V and by exceeding 172 V another zone of the anode starts to become affected and grows as voltage difference increases. The spread of the discolored area is roughly radial from the biasing voltage contact linking it to the field spreading across the dielectric substrate. Note that no streaks were generated in this experiment.

For the structure in Figure 5, the gap between the anode and cathode is 3 μm, for which a voltage of 152 V corresponds to an electric field of $\sim 50\,\mathrm{MVm^{-1}}$. This value is an underestimation ignoring the shape of the electrodes and is close the reported dielectric breakdown of STO.[29] Scanning electron microscopy images of the affected area clearly reveal evidence of gas bubbles developing under the anode, suggesting
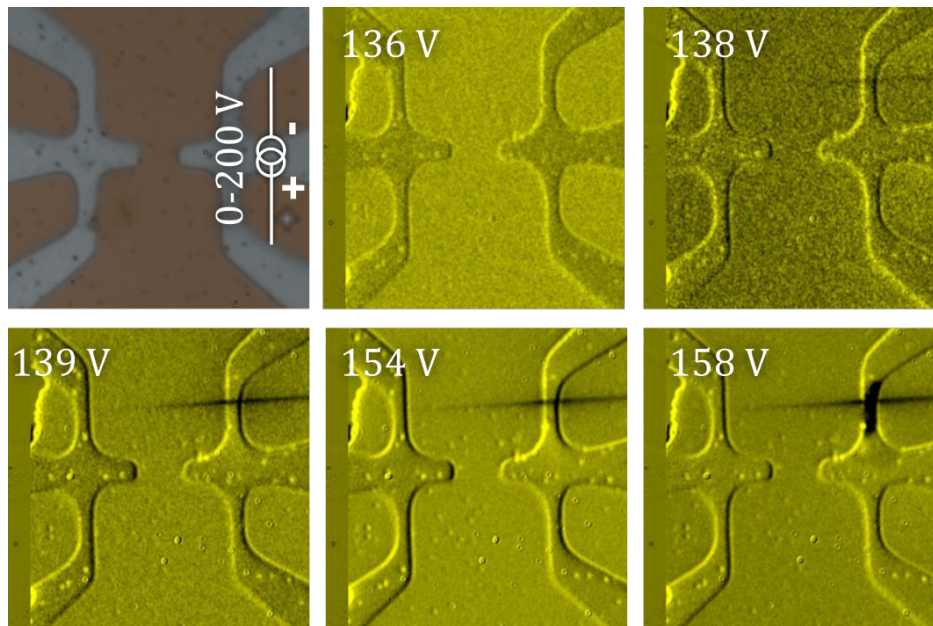
Figure 6: Upper left panel: Optical microscopy image of the measured device and the connection circuit used to sweep the voltage ranging from 0 to 200 V at ambient conditions. The narrowest gap between the two electrodes is 3 μm. Yellowish background panels show differential images for which the image of the pristine sample has been subtracted to that of the indicated voltage. A singular linear crystallographic defect develops and grows in the system above 138 V, before the device is electrically damaged at 158 V.

a solid-state electrolytic processes as reported by Szot et al.[24] More importantly, the absence of streaks as those reported in Ref.[24] confirms that the lines observed in Figure 4 have a different origin.

By changing the circuit configuration to that shown in **Figure 6** in such a way to induce a circulating current in the right side of the sample, we can reproducibly confirm the triggering of the linear structural defects at high applied voltages. A selected set of differential images acquired at the voltage labeled in each panel, shows that little happens to the sample up to 136 V and then from 138 V a linear structural defect develops and subsequently grows until 158 V, where the LSMO sample is locally damaged. Concomitant electric transport measurements along the current path show that the sudden appearance of the linear structural defect leads to a resistance jump. This is expected considering that the thickness of the LSMO is similar to the depth of the linear trench created in the substrate.

We have also simultaneously measured the leakage current through the gap by applying 1 V between the left and right side of the structure. Interestingly, within the noise level of the measurement, a nearly constant leakage current of 10 nA remains unaffected by the formation of the linear defect. This is yet another distinctive feature differing from the streaks reported in Ref.[24] Furthermore, by performing conducting-AFM in the structural steps and plateaus we confirm that these defects do not represent conducting channels. It is also worth mentioning that we were unable to trigger the linear defects in a similar device made of 100 nm-thick Ag (instead of LSMO). In this case, the electromigration of Ag happens at high currents ($\sim$ 41 mA), but overall low dissipated power (about 50 times lower than in LSMO) thus unable to reach the high temperature gradients needed to induce the linear fractures (see Supporting Information).

The optical images shown in Figure 6 show that the imprinted signature of the linear defects fades away as the distance from the nucleation point increases. In order to unveil the underlying mechanism of this effect, we resort to complementary ex situ SEM and AFM investigations of a comparable device as the one shown in Figure 6. These results are summarized in **Figure 7**. In panel (a), a SEM image of the region of interest reveals the presence of additional lines not resolved by the optical microscopy. The extent of two notable trenches on this sample were measured by AFM. The lines correspond to height steps measured along the directions x_1 and x_2 indicated in panel (a). The resulting step-height profiles are shown in panel (b) for the direction x_1 and in panel (c) for the direction x_2. These profiles show
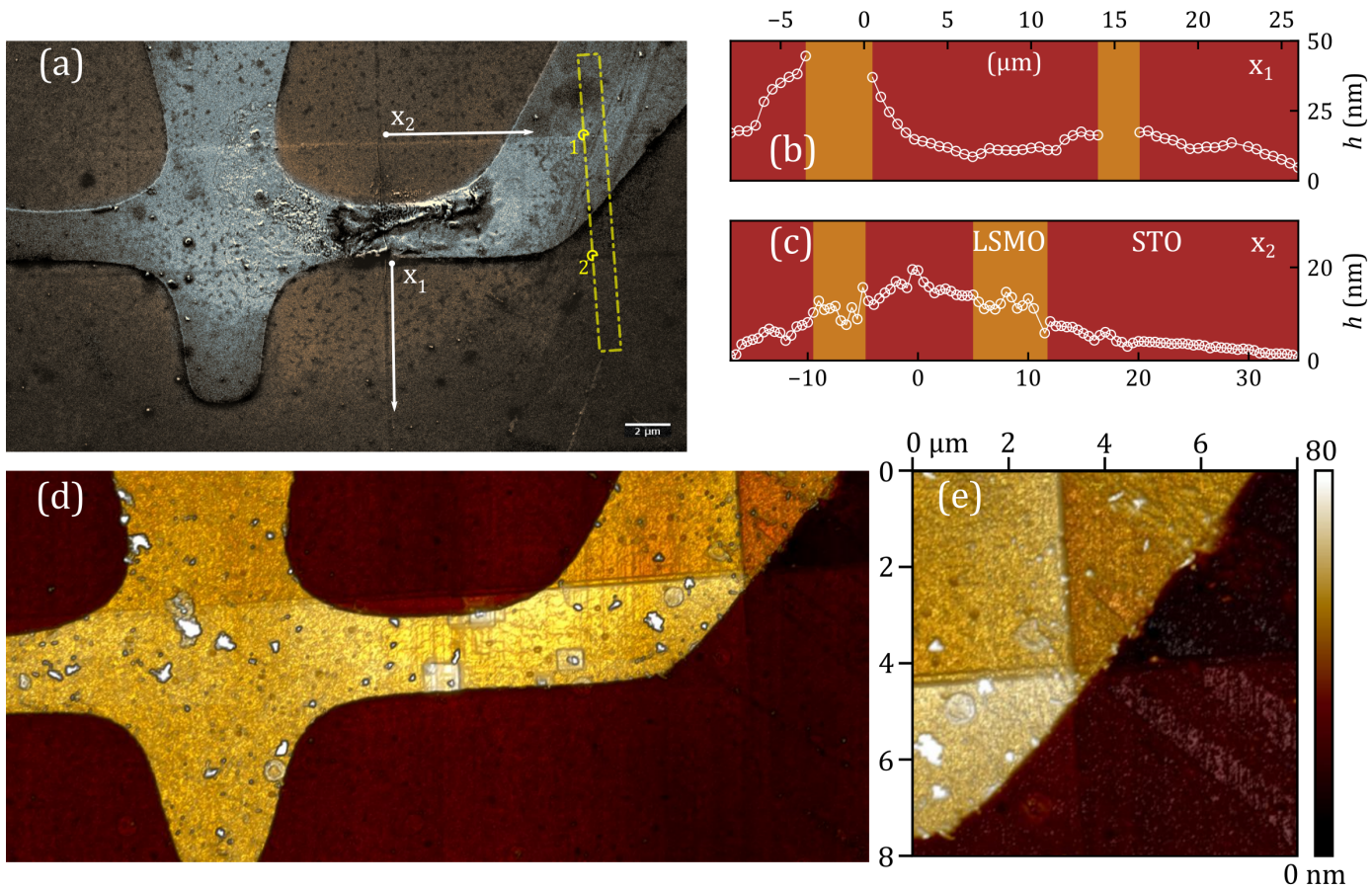
Figure 7: (a) Scanning electron microscopy of a LSMO/STO device evidencing several steps after severe electrothermal stress. Step-height along the x_1 (b) and along the x_2 (c) directions indicated in panel (a). Note that the profile along x_1 crosses two LSMO bridges, the one shown in (a) and one opposing it across the gap as shown in Figure 6. (d) Atomic force microscopy image of a device comparable to the one in (a) after triggering surface scars by applying electro-thermal stress. A zoom-in of the AFM images of the device in (b) at a crossing point of several lines is shown in panel (e). The rectangular box in panel (a) indicates the lamella cut-out by focused ion beam for subsequent STEM investigation presented in Figure 8 and Figure 9.

that the step-height decreases as the distance from the nucleation point (the LSMO nanoconstriction) increases, explaining the progressive fading of the lines observed optically in Figure 6. Another sample that underwent crystallographic deformation under electric bias was analyzed by AFM and is presented in panel (d). A zoom-in of the AFM images at a crossing point of several lines is shown in panel (e). These images evidence several step levels occurring on the STO substrate.

Considering the origin of the observed streaks, it is important to note that both LSMO and STO, as well as their interface are known to exhibit vacancy ordering driven phase transformations. Indeed, LSMO subjected to either heating, electric bias or epitaxial strain effects close to the substrate interface, shows vacancy ordering which leads to the formation of a new phase with a reduced unit cell[18] (brownmillerite[30] - $La_{0.7}Sr_{0.3}MnO_{2.5}$), while in STO, oxidizing conditions and electric bias are known to induce the formation of interwoven Ruddlesden-Popper phases (usually denoted $SrO(SrTiO_3)_n$ or $SrTiO_{2.5}$).[23,31] All of these phase changes lead to alterations in the unit cell parameter of the material. Oxygen vacancy ordering can also occur between these two materials, mostly due to their shared, large oxygen mobility and similar unit cell constants,[32,33] with some arguing for a limited oxygen exchange across the interface.[18] These previous results are, admittedly, hard to compare due to broadly varying sample history and methodologies, but it seems abundantly clear that both materials in our system can accommodate variable amounts of oxygen vacancies by making structural concessions. The importance of the epitaxial strain between the thin film and the substrate can not be ignored, as it can affect the phase composition close to the interface and
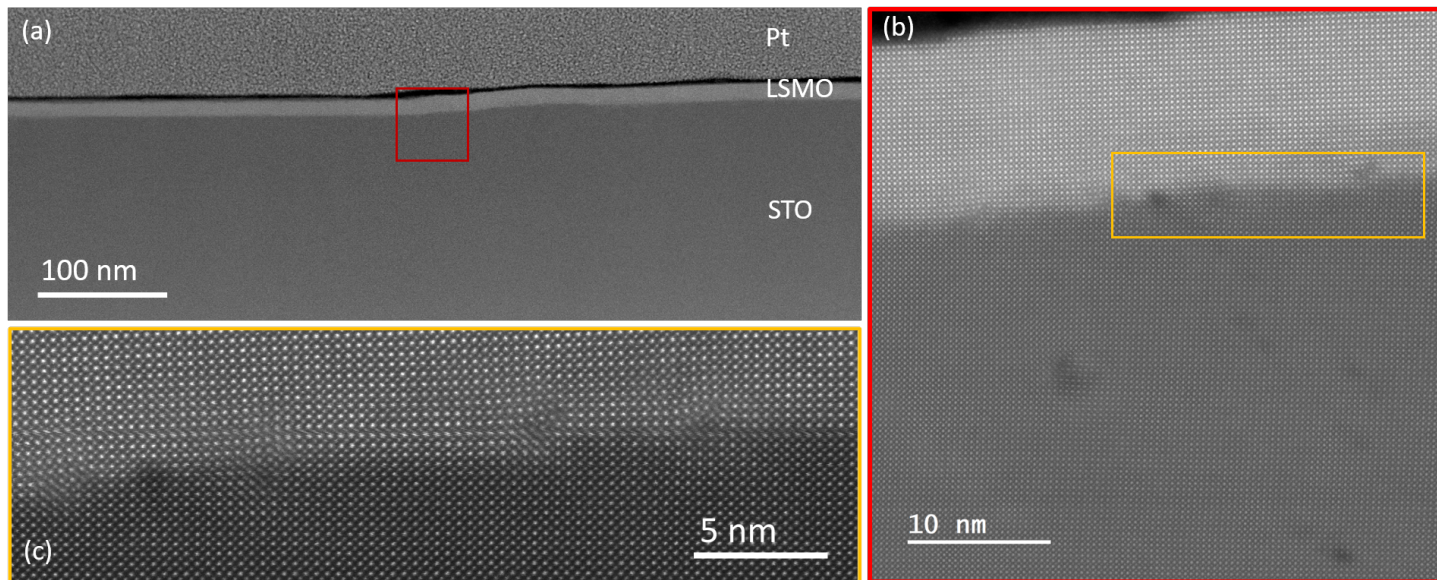
Figure 8: (a) Low magnification Z-contrast image of the FIB-cut lamella obtained from the zone indicated in Figure 7(a) around the step labeled 1. (b) Higher-magnification Z-contrat image of the red framed region marked in panel (a). (c) Atomic resolution image image of the yellow framed region marked in panel (b).

has been shown to increase vacancy mobility in perovskites.[34] Investigating the heat diffusion and electric field distribution on the proposed system with specific regard to vacancy distribution and sample geometry might give more clues on the species mobility in the case under study and allow us to gain insight into the thermodynamics of the effect at hand (see Support Information).

   In order to gain further insights on the crystallographic modifications induced both by electrically stimulated oxygen migration as well as by the formation of the superficial scarring, we have carried out STEM investigations. To that end, a lamella was cut out using a focused Ga-ion beam (FIB) in the region indicated in Figure 7(a). This region of interest includes two steps triggered by the electro-thermal effect indicated with the labels 1 and 2. **Figure 8** and **Figure 9** summarize the most salient features observed in the vicinity of the surface scars 1 and 2, respectively. In Figure 8(a) a low-magnification Z-contrast image evidences the presence of a Pt top layer used to protect the LSMO/STO during FIB cutting process. The LSMO appears brighter than the STO substrate because it contains a heavier cation (La). Figure 8(b) shows a higher-magnification Z-contrast image of the red-framed region marked in panel (a) where the step 1 takes place. Note that in this region the LSMO/STO interface exhibits several defects and the nearby LSMO planes are highly tilted. Interestingly, dark spots running along the (101) crystallographic direction, and likely arising from dislocations, are embedded within the STO.[35] The darkish contrast of these defects suggests an increase of the unit cell around them (i.e. Sr-Sr distance) and therefore a contrast decrease. The proliferation of edge dislocation at the LSMO/STO inferface is more apparent in panel (c) corresponding to the yellow framed region in panel (b). It is worth mentioning that the proliferation of these defects resulting from the electro-thermal stress is not visible away from the linear scars, where the LSMO layer shows a cube-on-cube epitaxial relationship with STO substrate and a coherent and sharp interface absent of defects.

   In Figure 9(a) a low-magnification Z-contrast image of the step 2 is shown, along with a higher-magnification image taken at the red-framed region (Figure 9(b)) and blue-framed region (Figure 9(c)). Note that at this step there is no LSMO layer on top. The presence of dislocations embedded in the STO and emerging from the surface step is confirmed in Figure 9(b). In this panel, the Z-contrast image shows clear atomic scale steps at the surface. Faint contrast along the (101) plane likely related to a distortion of the STO matrix become apparent in Figure 9(c). The defects found within the STO substrate shown in Fig. 8 and 9 run parallel to the (101) planes, which might correspond to the gliding planes, see Fig. 4 of the Supporting Information. Simultaneously acquired Electron Energy Loss Spectroscopy (EELS) reveals no significant changes in the fine structure of the Ti and Mn L-edges and the O K-edges of both
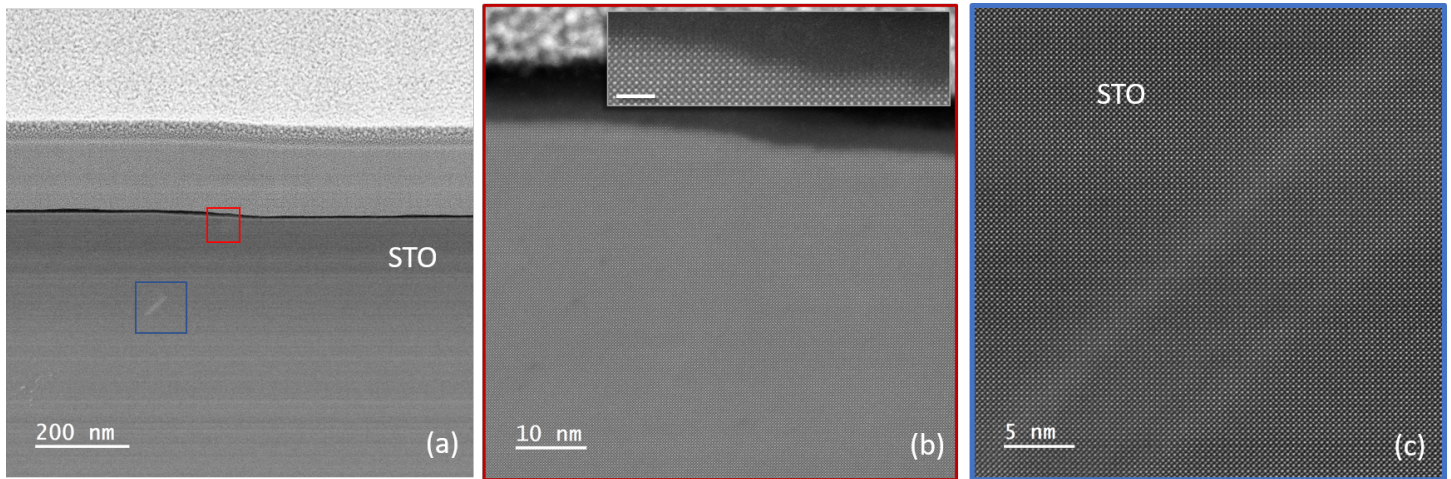
Figure 9: (a) Low magnification *Z*-contrast image of the FIB-cut lamella obtained from the zone indicated in Figure 7(a) around the step labeled 2 .(b,c) Higher-magnification *Z*-contrat image of the red and blue framed regions marked in panel (a), respectively. Inset in (b) shows an enlarged image at the surface of the bare STO. Scale bar is 2 nm long.

the LSMO layer and the STO substrate when comparing regions at the steps/defects and far from them (see Supporting Information). This finding suggests that the scars do not involve oxygen vacancies far from the nucleation point.

We speculate that the pair of scars and the consequent proliferation of defects favor gliding planes along the (101) direction because of the shorter atomic distance along these planes (corresponding to lower activation energy for atomic diffusion). The fact that no correlated defects are observed in the manganite layer is consistent with a high temperature during the electro-thermal formation and the consequent plastic deformation of this layer. Nevertheless, the highest reached temperature does not seem to be enough to promote large diffusion of oxygen across the LSMO/STO interface. This interpretation is consistent with the early report by Jiang et al.[36] on the thermo-mechanical plastic deformation in resistive switching devices made of vertical structures with Pt electrodes on oxygen depleted STO samples.

3   Conclusion

The main finding of this work is twofold. Firstly, we demonstrate, by means of concurrent optical imaging and electrical characterization, the directional nature of electrically stimulated oxygen displacement in LSMO. Evidence for this is found in the directional resistive switching noted around the nucleation point of electromigration and in real-time optical images which reveal a vacancy-rich propagating front spreading on the cathode side of a LSMO nanoconstriction. This observation goes along with the wealth of evidence for enhanced oxygen mobility in perovskite-like solid systems and speaks for the potential electromigration holds to tailor the material properties.

Secondly, we show that at higher applied voltages, an interplay of vacancy ordering, electromigration and thermal effects causes extended changes in both the studied thin film and the STO substrate. This manifests as crystallographically aligned steps in the topography of the observed samples, originating at the conductive LSMO strip and extending along the STO wafer axes up to ∼30 μm away. HRSTEM imaging provides valuable hints to elucidate the origin of this superficial scarring and suggests a scenario where local electro-thermal stress generated under the narrowest section of the LSMO sample, is released by the generation of edge dislocations running along the crystallographic (101) direction of the STO substrate. We demonstrate that the observed linear steps are reproducible and precede dielectric breakdown of the system and do not correspond to electroformed conduction channels as reported in previous works.[24]

Electrically-controlled oxygen migration is at the heart of some of the most interesting resistive switching complex oxide systems, as well as offering a new window into the study of material's phase diagrams as samples with engineered vacancy distributions can be created and tuned in situ. The investigated system

coupled with its specific physical properties, like the magnetoresistance in LSMO, can be used as the basis for applications in memory and sensing, as well as offering a way to prepare switches or integrators for future electronics. Controlled defect introduction into a material, separated or coupled with atomic migration effects could allow to surpass bulk doping limits when properly controlled, as shown in recent literature.[37,38] In this sense, further study and mastery over the above reported defect generation procedure seems invaluable to attain further progress in device functionalization.

4 Experimental Section

Sample Fabrication:

The $La_{0.7}Sr_{0.3}MnO_3$ thin films studied in this work were epitaxially grown by polymer-assisted deposition (PAD) on (001)-SrTiO$_3$ single-crystal substrates.[39] Individual solutions of the different metal ions were prepared by dissolving the corresponding La, Sr and Mn nitrates in water with ethylenediaminetetraacetic acid (EDTA, 1:1 molar ratio) and polyethilenimine (PEI), Sigma Aldrich Ref. 408727, with an average molecular weight of 25.000 (1:1 mass ratio to EDTA). Each individual solution was filtrated using Amicon filtration units (10 kDa), and retained portions were analyzed by Inductively Coupled Plasma (ICP) Spectrometry (Optima 4300 DV ICP-OES Perkin-Elmer). Solutions were mixed according to the desired stoichiometry (La:Sr:Mn=0.7:0.3:1) and spin-coated on top of 5×5 mm^2 (001)-STO substrates purchased from CrysTec GmbH, Germany. After the polymeric layer has been deposited, it is annealed in a horizontal tube furnace in oxygen flow at 950 °C for 90 min. The thickness of the grown LSMO epitaxial thin films was $12-20$ nm as determined by X-ray reflectometry. The LSMO thin films were subsequently patterned by photolithography and dry ion-beam etching. The etching process etches away the uncovered LSMO film and a few tenths of nm of the STO substrate. For ensuring ohmic electrical contacts, 50-100 nm thick Ag electrodes were sputtered and annealed by heating in an oxygen-rich environment.

Optical Imaging:

Optical microscopy was performed using an Olympus polarized light microscope outfitted with a green-filtered mercury lamp. Objectives of $20\times$ (Numerical aperture - NA 0.4) and $50\times$ (NA 0.5) magnification were used per demand and digital images were captured with a charge-coupled device (CCD) digital camera, software-controlled by means of a LabVIEW virtual instrument. Multiple images are taken (exposure times in the ms range) and averaged, then post-processed using ImageJ and home-made python scripts.

Scanning Transmission Electrom Microscopy:

Aberration-corrected scanning transmission electron microscopy (STEM) was used for microstructural analysis with atomic resolution. Samples were characterized using a JEOL JEM ARM200cF operated at 200 kV, equipped with a CEOS aberration corrector and GIF Quantum ER spectrometer, at the Universidad Complutense de Madrid, Spain. When acquired in high-angle annular dark-field imaging mode (HAADF), the STEM images show the so-called Z-contrast, where the intensity of the atomic columns scales with the atomic number Z. The STEM specimens were prepared using a FEI Helios nanolab 650, at SEM-FIB microscopy service of the Universidad de Málaga.

References

[1] A. Asamitsu, Y. Tomioka, H. Kuwahara, Y. Tokura, *Nature* **1997**, *388*, 6637 50.

[2] Y. B. Nian, J. Strozier, N. J. Wu, X. Chen, A. Ignatiev, *Phys. Rev. Lett.* **2007**, *98*, 14 3.

[3] M. A. Peña, J. L. Fierro, *Chem. Rev.* **2001**, *101*, 7 1981.

[4] Z. Shao, S. M. Haile, *Mater. Sustain. Energy A* **2010**, *3*, 1978 255.

[5] M. B. Salamon, M. Jaime, *Rev. Mod. Phys.* **2001**, *73*, 3 583.

[6] E. Dagotto, T. Hotta, A. Moreo, *Phys. Rep.* **2001**, *344*, 1-3 1.

[7] F. Gunkel, D. V. Christensen, Y. Z. Chen, N. Pryds, *Appl. Phys. Lett.* **2020**, *116*, 12.

[8] M. Søgaard, P. Vang Hendriksen, M. Mogensen, *J. Solid State Chem.* **2007**, *180*, 4 1489.

[9] A. Urushibara, Y. Moritomo, T. Arima, A. Asamitsu, G. Kido, Y. Tokura, *Phys. Rev. B* **1995**, *51*, 20 14103.

[10] S. V. Kalinin, N. A. Spaldin, *Science* **2013**, *341*, 6148 858.

[11] C. Zener, *Phys. Rev.* **1951**, *82*, 3 403.

[12] H. L. Ju, J. Gopalakrishnan, J. L. Peng, Q. Li, G. C. Xiong, T. Venkatesan, R. L. Greene, *Phys. Rev. B* **1995**, *51*, 9 6143.

[13] L. Balcells, L. Peña, R. Galceran, A. Pomar, B. Bozzo, Z. Konstantinovic, F. Sandiumenge, B. Martinez, *J. Appl. Phys.* **2013**, *113*, 7.

[14] J. Li, J. Wang, H. Kuang, H. R. Zhang, Y. Y. Zhao, K. M. Qiao, F. Wang, W. Liu, W. Wang, L. C. Peng, Y. Zhang, R. C. Yu, F. X. Hu, J. R. Sun, B. G. Shen, *Nanoscale* **2017**, *9*, 35 13214.

[15] G. Lin, H. Wang, X. Cai, W. Tong, H. Zhu, *AIP Adv.* **2020**, *10*, 5 1.

[16] J. C. Gonzalez-Rosillo, S. Catalano, I. Maggio-Aprile, M. Gibert, X. Obradors, A. Palau, T. Puig, *Small* **2020**, *16* 2001307.

[17] P. M. Chowdhury, A. K. Raychaudhuri, *Mater. Res. Bull.* **2021**, *137*, November 2020.

[18] L. Yao, S. Inkinen, S. Van Dijken, *Nat. Commun.* **2017**, *8* 1.

[19] S. Marinković, A. Fernandez-Rodriguez, S. Collienne, S. Blanco Alvarez, S. Melinte, B. Maiorov, G. Rius, X. Granados, N. Mestres, A. Palau, A. V. Silhanek, *ACS Nano* **2020**, *14*, 9 11765.

[20] J. Hanzig, M. Zschornak, F. Hanzig, E. Mehner, H. Stöcker, B. Abendroth, C. Röder, A. Talkenberger, G. Schreiber, D. Rafaja, S. Gemming, D. C. Meyer, *Phys. Rev. B - Condens. Matter Mater. Phys.* **2013**, *88*, 2 1.

[21] H. Gao, S. Sahu, C. A. Randall, L. J. Brillson, *J. Appl. Phys.* **2020**, *127*, 094105.

[22] T. Leisegang, H. Stöcker, A. A. Levin, T. Weißbach, M. Zschornak, E. Gutmann, K. Rickers, S. Gemming, D. C. Meyer, *Phys. Rev. Lett.* **2009**, *102*, 8 1.

[23] M. Bobeth, N. Farag, A. A. Levin, D. C. Meyer, W. Pompe, A. E. Romanov, *J. Ceram. Soc. Japan* **2006**, *114*, 1335 1029.

[24] K. Szot, W. Speier, G. Bihlmayer, R. Waser, *Nat. Mater.* **2006**, *5*, 4 312.

[25] R. Waser, R. Dittmann, C. Staikov, K. Szot, *Adv. Mater.* **2009**, *21*, 25-26 2632.

[26] C. Rodenbücher, S. Menzel, D. Wrana, T. Gensch, C. Korte, F. Krok, K. Szot, *Sci. Rep.* **2019**, *9*, 1 1.

[27] V. Metlenko, A. H. H. Ramadan, F. Funkel, H. Du, H. Schraknepper, S. Hoffmann-Eifert, R. Dittmann, R. Waser, R. A. De Souza, *Nanoscale* **2014**, *6* 12864.

[28] D. Marrocchelli, L. Sun, B. Yildiz, *J. Am. Chem. Soc.* **2015**, *137* 4735.

[29] H. H. Barrett, *J. Appl. Phys.* **1964**, *35*, 5 1420.

[30] T. G. Parsons, H. D'Hondt, J. Hadermann, M. A. Hayward, *Chem. Mater.* **2009**, *21*, 22 5527.

[31] D. C. Meyer, A. A. Levin, T. Leisegang, E. Gutmann, P. Paufler, M. Reibold, W. Pompe, *Appl. Phys. A Mater. Sci. Process.* **2006**, *84*, 1-2 31.

[32] M. Nord, P. E. Vullum, M. Moreau, J. E. Boschker, S. M. Selbach, R. Holmestad, T. Tybell, *Appl. Phys. Lett.* **2015**, *106*, 4 0.

[33] S. Koohfar, A. S. Disa, M. S. J. Marshall, F. J. Walker, C. H. Ahn, D. P. Kumah, *Phys. Rev. B* **2017**, *024108* 6.

[34] T. Mayeshiba, D. Morgan, *Phys. Chem. Chem. Phys.* **2015**, *17*, 4 2715.

[35] Z. Zhang, W. Sigle, M. Rühle, *Phys. Rev. B* **2002**, *66* 094108.

[36] W. Jiang, R. J. Kamaladasa, Y. M. Lu, A. Vicari, R. Berechman, P. A. Salvador, J. A. Bain, Y. N. Picard, M. Skowronski, *J. App. Phys.* **2011**, *110*, 5.

[37] M. D. Armstrong, K. W. Lan, Y. Guo, N. H. Perry, *ACS Nano* **2021**, *15*, 6 9211.

[38] D. M. Evans, D. Ren, T. S. Holstad, P. E. Vullum, A. B. Mosberg, Z. Yan, E. Bourret, A. T. J. V. Helvoort, S. M. Selbach, D. Meier, *Nano Lett.* **2021**, *21* 3386.

[39] H. Wang, C. Frontera, J. Herrero-Martín, A. Pomar, P. Roura, B. Martínez, N. Mestres, *Chem. - A Eur. J.* **2020**, *26*, 42 9338.

Table of Contents
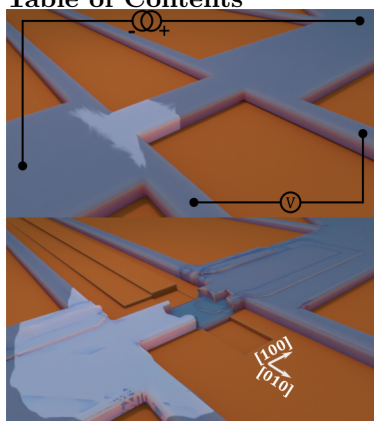
The authors modulate the oxygen doping levels in $La_{0.7}Sr_{0.3}MnO_3$ (LSMO) nanobridges grown on $SrTiO_3$ (STO) substrates by means of electric current. The effects of the treatment extend beyond resistive switching to induce highly localized crystallographic defects in the STO substrate via heating.